

# Common quantum phase transition in quasicrystals and heavy-fermion metals

V. R. Shaginyan,<sup>1,2,\*</sup> A. Z. Msezane,<sup>2</sup> K. G. Popov,<sup>3</sup> G. S. Japaridze,<sup>2</sup> and V. A. Khodel<sup>4,5</sup>

<sup>1</sup>*Petersburg Nuclear Physics Institute, Gatchina, 188300, Russia*

<sup>2</sup>*Clark Atlanta University, Atlanta, GA 30314, USA*

<sup>3</sup>*Komi Science Center, Ural Division, RAS, Syktyvkar, 167982, Russia*

<sup>4</sup>*Russian Research Centre Kurchatov Institute, Moscow, 123182, Russia*

<sup>5</sup>*McDonnell Center for the Space Sciences & Department of Physics,  
Washington University, St. Louis, MO 63130, USA*

Extraordinary new materials named quasicrystals and characterized by noncrystallographic rotational symmetry and quasiperiodic translational properties have attracted scrutiny. Study of quasicrystals may shed light on the most basic notions related to the quantum critical state observed in heavy-fermion metals. We show that the electronic system of some quasicrystals is located at the fermion condensation quantum phase transition without tuning. In that case the quasicrystals possess the quantum critical state with the non-Fermi liquid behavior which in magnetic fields transforms into the Landau Fermi-liquid one. Remarkably, the quantum critical state is robust despite the strong disorder experienced by the electrons. We also demonstrate for the first time that quasicrystals exhibit the typical scaling behavior of their thermodynamic properties such as the magnetic susceptibility, and belong to the famous family of heavy-fermion metals. Our calculated thermodynamic properties are in good agreement with recent experimental observations.

PACS numbers: 71.23.Ft, 71.27.+a, 05.30.Rt

When encountering exciting behavior of strongly correlated metals, we anticipate to learn more about quantum critical physics. Such an opportunity may be provided by quasicrystals (QCs)<sup>1</sup>. These, characterized by the absence of translational symmetry in combination with good atomic arrangement and rotational symmetry, can be viewed as materials located between crystalline and disordered solids. QCs, approximants and related complex metallic phases reveal very unusual mechanical, magnetic, electronic transport and thermodynamic properties. The aperiodicity of QCs plays an important role at the formation of the properties since the band electronic structure governed by the Bloch theorem cannot be well defined. As an example, QCs exhibit a high resistivity although the density of states (DOS) at the Fermi energy is not small<sup>2</sup>. One expects transport properties to be defined by a small diffusivity of electrons which occupy a new class of states denoted as "critical states", neither being extended nor localized, and making the velocity of charge carriers very low<sup>2</sup>. Associated with these critical states, characterized by an extremely degenerate confined wave function, are the so-called "spiky" DOS<sup>3,4</sup>. These predicted DOS are corroborated by experiments revealing that single spectra of the local DOS demonstrate a spiky DOS<sup>5,6</sup>. Clearly these spiky states are associated with flat bands<sup>7,8</sup>. On one hand, we expect the properties related to the itinerate states governed by the spiky states of QCs to coincide with that of heavy-fermion metals, while on the other hand, the pseudo localized states may result in those of amorphous materials. Therefore, the question of how quasicrystalline order influences the electronic properties in quasicrystals, whether these resemble those of heavy-fermion (HF) metals or those of amorphous materials, is of crucial importance.

Recently, experimental measurements on the gold-

aluminium-ytterbium quasicrystal  $\text{Au}_{51}\text{Al}_{34}\text{Yb}_{15}$  with a six-dimensional lattice parameter  $a_d = 0.7448$  nm have revealed a quantum critical behavior with the unusual exponent  $\alpha \simeq 0.51$  defining the divergency of the magnetic susceptibility  $\chi \propto T^{-\alpha}$  as temperature  $T \rightarrow 0$ <sup>9</sup>. The measurements have also exposed that the observed non-Fermi liquid (NFL) behavior transforms into Landau Fermi liquid (LFL) under the application of a tiny magnetic field  $H$ , while it exhibits the robustness against hydrostatic pressure; the quasicrystal shows also metallic behavior with the  $T$ -dependent part  $\Delta\rho$  of the resistivity,  $\Delta\rho \propto T$ , at low temperatures<sup>9</sup>. All these facts challenge theory to explain a quantum criticality of the gold-aluminum-ytterbium QC characterized by the unusual exponent and robust against hydrostatic pressure but destroyed by tiny magnetic fields.

In this communication we uncover that a quantum critical point of  $\text{Au}_{51}\text{Al}_{34}\text{Yb}_{15}$ , generating the NFL behavior, is a fermion condensation quantum phase transition (FCQPT)<sup>10,11</sup> and also present the first explanation of the low temperature thermodynamics in magnetic fields. We explain the robustness of the quantum critical behavior against the hydrostatic pressure, and how the application of a weak magnetic field destroys the behavior and makes the system transit from the NFL to LFL behavior. We also demonstrate that there is a general mechanism underlying the NFL behavior of HF metals and quasicrystals, leading to a scaling behavior.

We start with constructing a model to explain the challenging behavior of the gold-aluminum-ytterbium QC. Taking into account that the spiky states are associated to flat bands<sup>7</sup> which are the generic signature of FCQPT, we safely assume that the electronic system of the gold-aluminum-ytterbium QC  $\text{Au}_{51}\text{Al}_{34}\text{Yb}_{15}$  is located very near FCQPT<sup>10</sup>. Thus,  $\text{Au}_{51}\text{Al}_{34}\text{Yb}_{15}$  turns out to be lo-

cated at FCQPT without tuning this substance with the pressure, magnetic field etc. We expect that the system exhibits the robustness of its critical behavior against the hydrostatic pressure since the hydrostatic pressure does not change the topological structure of QC leading to the spiky DOS and, correspondingly, flat bands. As we will see, the spiky DOS cannot prevent the field-induced Fermi liquid state.

To study the low temperature thermodynamic and scaling behavior, we use the model of homogeneous heavy-fermion liquid<sup>10</sup>. This model avoids the complications associated with the anisotropy of solids and considering both the thermodynamic properties and NFL behavior by calculating the effective mass  $M^*(T, H)$  as a function of temperature  $T$  and magnetic field  $H$ . To study the behavior of the effective mass  $M^*(T, H)$ , we use the Landau equation for the quasiparticle effective mass. The only modification is that in our formalism the effective mass is no longer constant but depends on temperature and magnetic field. For the model of homogeneous HF liquid at finite temperatures and magnetic fields, this equation takes the form<sup>10-13</sup>

$$\frac{1}{M^*(T, H)} = \frac{1}{M} + \sum_{\sigma_1} \int \frac{\mathbf{p}_F \mathbf{p}}{p_F^3} F_{\sigma, \sigma_1}(\mathbf{p}_F, \mathbf{p}) \times \frac{\partial n_{\sigma_1}(\mathbf{p}, T, H)}{\partial p} \frac{d\mathbf{p}}{(2\pi)^3}, \quad (1)$$

where  $M$  is a bare electron mass,  $F_{\sigma, \sigma_1}(\mathbf{p}_F, \mathbf{p})$  is the Landau interaction, which depends on Fermi momentum  $p_F$ , momentum  $p$  and spin  $\sigma$ . Here we use the units where  $\hbar = k_B = 1$ . The Landau interaction has the form<sup>13</sup>

$$F_{\sigma, \sigma'}(\mathbf{p}, \mathbf{p}') = \frac{\delta^2 E[n]}{\delta n_{\sigma}(\mathbf{p}) \delta n_{\sigma'}(\mathbf{p}')}, \quad (2)$$

where  $E[n]$  is the system energy, which is a functional of the quasiparticle distribution function  $n$ <sup>10,12,13</sup>. It can be expressed as

$$n_{\sigma}(\mathbf{p}, T) = \left\{ 1 + \exp \left[ \frac{(\varepsilon(\mathbf{p}, T) - \mu_{\sigma})}{T} \right] \right\}^{-1}, \quad (3)$$

where  $\varepsilon(\mathbf{p}, T)$  is the single-particle spectrum. In our case, the chemical potential  $\mu$  depends on the spin due to Zeeman splitting  $\mu_{\sigma} = \mu \pm \mu_B H$ ,  $\mu_B$  is Bohr magneton. The single-particle spectrum is a variational derivative of the system energy  $E[n_{\sigma}(\mathbf{p})]$  with respect to the quasiparticle distribution function or occupation numbers  $n$ ,

$$\varepsilon(\mathbf{p}) = \frac{\delta E[n(\mathbf{p})]}{\delta n}. \quad (4)$$

In our case  $F$  is fixed by the condition that the system is situated at FCQPT. The variational procedure, being applied to the functional  $E[n_{\sigma}(\mathbf{p}, T)]$ , gives using the form for  $\varepsilon(\mathbf{p}, T) = \varepsilon_{\sigma}(\mathbf{p}, T) \equiv \varepsilon[n_{\sigma}(\mathbf{p}, T)]$ ,

$$\frac{\partial \varepsilon_{\sigma}(\mathbf{p}, T)}{\partial \mathbf{p}} = \frac{p}{M} + \sum_{\sigma_1} \int F_{\sigma, \sigma_1}(\mathbf{p}, \mathbf{p}_1) \frac{\partial n_{\sigma_1}(\mathbf{p}_1, T)}{\partial \mathbf{p}} \frac{d^3 p_1}{(2\pi)^3}. \quad (5)$$

Equations (3) and (5) constitute the closed set for self-consistent determination of  $\varepsilon_{\sigma}(\mathbf{p}, T)$  and  $n_{\sigma}(\mathbf{p}, T)$ . The sole role of the Landau interaction is to bring the system to FCQPT point, where  $M^* \rightarrow \infty$  at  $T = 0$  and  $H = 0$ , and the Fermi surface alters its topology so that the effective mass acquires temperature and field dependence<sup>10-12,14</sup>. Provided that the Landau interaction is an analytical function, at the Fermi surface the momentum-dependent part of the Landau interaction can be taken in the form of truncated power series  $F = aq^2 + bq^3 + cq^4 + \dots$ , where  $\mathbf{q} = \mathbf{p}_1 - \mathbf{p}_2$ ,  $a, b$  and  $c$  are fitting parameters which are defined by the condition that the system is at FCQPT. Close to the Fermi momentum  $p_F$ , the electron spectrum  $\varepsilon(p)$ , given by Eq. (5) with the above interaction  $F$ , behaves as  $\varepsilon(p) - \mu \propto (p - p_F)^3$ <sup>10,14</sup>. A direct inspection of Eq. (1) shows that at  $T = 0$  and  $H = 0$ , the sum of the first term and the second one on the right side vanishes, since  $1/M^*(T \rightarrow 0) \rightarrow 0$  provided that the system is located at FCQPT<sup>10,14</sup>. In case of analytical Landau interaction at finite  $T$  the right hand side is proportional  $F'(M^*)^2 T^2$ , where  $F'$  is the first derivative of  $F$  with respect to  $q$  at  $q \rightarrow 0$ . Calculations of the corresponding integrals can be found in textbooks, see e.g.<sup>15</sup> Thus, we have  $1/M^* \propto (M^*)^2 T^2$ , and obtain<sup>10,14</sup>

$$M^*(T) \simeq a_T T^{-2/3}. \quad (6)$$

At finite  $T$ , the application of magnetic field  $H$  drives system to the LFL region with

$$M^*(H) \simeq a_H H^{-2/3}. \quad (7)$$

On the other hand, an analytic interaction  $F$  can lead to the general topological form of the spectrum  $\varepsilon(p) - \mu \propto (p - p_b)^2 (p - p_F)$  with  $(p_b < p_F)$  and  $(p_F - p_b)/p_F \ll 1$ , that makes  $M^* \propto T^{-1/2}$ , and creates a quantum critical point<sup>16</sup>. As we shall see below, the same critical point is generated by the interaction  $F(q)$  represented by an integrable over  $x$  nonanalytic function with  $q = \sqrt{p_1^2 + p_2^2 - 2xp_1p_2}$  and  $F(q \rightarrow 0) \rightarrow \infty$ <sup>10,17</sup>. The both cases lead to  $M^* \propto T^{-1/2}$ , and Eq. (6) becomes

$$M^*(T) \simeq a_T T^{-1/2}. \quad (8)$$

In the same way, we obtain

$$M^*(H) \simeq a_H H^{-1/2}, \quad (9)$$

with  $a_T$  and  $a_H$  are parameters. Taking into account that Eq. (8) leads to the spiky DOS with the vanishing of spiky structure with increasing temperature<sup>18</sup>, as it is observed in quasicrystals<sup>6,9</sup>, we assume that the general form of  $\varepsilon(p)$  produces the behavior of  $M^*$ , given by Eqs. (8) and (9), and is realized in quasicrystals which can be viewed as a generalized form of common crystals<sup>19</sup>. We note that the behavior  $1/M^* \propto \chi^{-1} \propto T^{1/2}$  is in good agreement with  $\chi^{-1} \propto T^{0.51}$  observed experimentally<sup>9</sup>. Our explanation is consistent with the robustness of the exponent 0.51 against the hydrostatic pressure<sup>9</sup> since the robustness is guaranteed by the

unique singular DOS of QCs that survives under the application of pressure<sup>3,4,6,7,9</sup>. Then, the nonanalytic Landau interaction can also serve as the good approximation, generating the observed behavior of the effective mass. We speculate that the nonanalytic interaction is generated by the nonconservation of the quasimomentum in QCs, making the Landau interaction  $F(q)$  a nonlocal function of momentum  $q$ . Such a function can be approximated by a nonanalytic one.

A few remarks on the transport properties of QC are in order here. In calculations of low-temperature resistivity, we employ a two-band model, one of which is occupied by heavy quasiparticles, with the effective mass given by Eq. (8), while the second band possesses a LFL quasiparticles with a  $T$ -independent effective mass<sup>20</sup>. As a result, we find that the quasiparticles width  $\gamma \propto T$  and that the  $T$ -dependent part of the resistivity  $\Delta\rho \propto T$ . This observation is in accordance with experimental facts<sup>9</sup>.

At finite  $H$  and  $T$  near FCQPT, the solutions of Eq. (1)  $M^*(T, H)$  can be well approximated by a simple universal interpolating function. A deeper insight into the behavior of  $M^*(T, H)$  can be achieved using some "internal" scales. Namely, near FCQPT the solutions of Eq. (1) exhibit a universal scaling behavior so that  $M^*(T, H)$  reaches its maximum value  $M_M^*$  at some temperature  $T_{\max} \propto H^{10,14}$ . It is convenient to introduce the internal scales  $M_M^*$  and  $T_{\max}$  to measure the effective mass and temperature, respectively. Thus, we divide the effective mass  $M^*$  and the temperature  $T$  by their maximal values,  $M_M^*$  and  $T_{\max}$  respectively. This generates the normalized effective mass  $M_N^* = M^*/M_M^*$  and temperature  $T_N = T/T_{\max}$ <sup>10</sup>. Near FCQPT the normalized solution of Eq. (1)  $M_N^*(T_N)$  with a nonanalytic Landau interaction can be well approximated by a simple universal interpolating function. The interpolation occurs between the LFL ( $M^* \propto a + bT^2$ ) and NFL ( $M^* \propto T^{-1/2}$ ) regimes and represents the universal scaling behavior of  $M_N^*(T_N)$

$$M_N^*(T_N) \approx c_0 \frac{1 + c_1 T_N^2}{1 + c_2 T_N^{5/2}}. \quad (10)$$

Here  $a$  and  $b$  are constants,  $c_0 = (1 + c_2)/(1 + c_1)$ ,  $c_1$  and  $c_2$  are fitting parameters. The inset to the left panel of Fig. 1 shows the scaling behavior of the normalized effective mass. It is seen from the inset, that the common width  $W$  of the LFL and the transition region  $W \propto T$  vanish as  $H \rightarrow 0$  since  $T_{\max} \propto H$ . In the same way, the common width of the NFL and the transition region tends to zero as soon as  $T \rightarrow 0$ .

Now we construct the schematic phase diagram of the gold-aluminum-ytterbium QC  $\text{Au}_{51}\text{Al}_{34}\text{Yb}_{15}$ . The phase diagram is reported in Fig. 1, left panel. The magnetic field  $H$  plays the role of the control parameter, driving the system outwards FCQPT that occurs at  $H = 0$  and  $T = 0$  without tuning since the QC critical state is formed by singular density of states<sup>3,4,6,7,9</sup>. It follows from Eq. (10) and seen from the left panel of Fig. 1, that

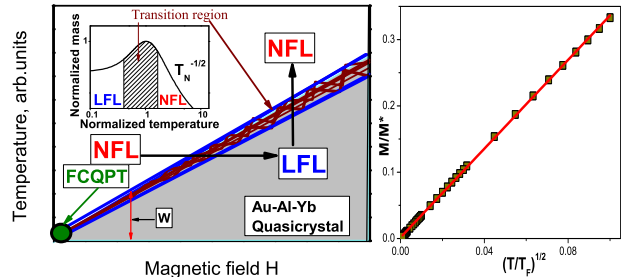


FIG. 1: (color online). Left panel.  $T - H$  phase diagram of  $\text{Au}_{51}\text{Al}_{34}\text{Yb}_{15}$  versus magnetic field  $H$  as the control parameter. The vertical and horizontal arrows show LFL-NFL and NFL-LFL transitions at fixed  $H$  and  $T$  respectively. At  $H = 0$  and  $T = 0$  the system is at FCQPT shown by the solid circle. The common width of the LFL and the transition regions  $W \propto T$  are shown by the double arrows. Inset shows a schematic plot of the normalized effective mass versus the normalized temperature. Transition region, where  $M_N^*$  reaches its maximum at  $T/T_{\max} = 1$ , is shown by the hatched area. The right panel reports the dimensionless inverse effective mass  $M/M^*$  versus dimensionless temperature  $(T/T_F)^{1/2}$ . The line is a linear fit.

at fixed temperatures the increase of  $H$  drives the system along the horizontal arrow from NFL state to LFL one. On the contrary, at fixed magnetic field and increasing temperatures the system transits along the vertical arrow from LFL state to NFL one. The inset to the left panel demonstrates the behavior of the normalized effective mass  $M_N^*$  versus normalized temperature  $T_N$  following from Eq. (10). The  $T^{-1/2}$  regime is marked as NFL since contrary to the LFL case, where the effective mass is constant, the effective mass depends strongly on temperature. It is seen that the temperature region  $T_N \sim 1$  signifies a transition regime between the LFL behavior with almost constant effective mass and the NFL one, given by  $T^{-1/2}$  dependence. Thus, temperatures  $T \simeq T_{\max}$ , shown by arrows in the inset and the main panel, can be regarded as the transition regime between LFL and NFL states. The common width  $W$  of the LFL transition regions  $W \propto T$  is shown by the heavy arrow. These theoretical results are in good agreement with the experimental facts<sup>9</sup>. The right panel of Fig. 1 illustrates the behavior of the dimensionless inverse effective mass  $M/M^*$  versus the dimensionless temperature  $(T/T_F)^{1/2}$ , where  $T_F$  is the Fermi temperature of electron gas. To calculate  $M/M^*$ , we use a model Landau functional<sup>10,17</sup>

$$E[n(\mathbf{p})] = \int \frac{\mathbf{p}^2}{2M} \frac{d\mathbf{p}}{(2\pi)^3} + \frac{1}{2} \int V(\mathbf{p}_1 - \mathbf{p}_2) \times n(\mathbf{p}_1)n(\mathbf{p}_2) \frac{d\mathbf{p}_1 d\mathbf{p}_2}{(2\pi)^6}, \quad (11)$$

with the Landau interaction

$$V(\mathbf{p}) = g_0 \frac{\exp(-\beta_0 \sqrt{\mathbf{q}^2 + \gamma^2})}{\sqrt{\mathbf{q}^2 + \gamma^2}}, \quad (12)$$

where the parameters  $g_0$  and  $\beta_0$  are fixed by the requirement that the system be located at FCQPT. The interaction at  $\gamma = 0$  becomes nonanalytic. It is worthy of note that the other nonanalytic interactions lead to the same behavior of  $M/M^*$ , see e.g.<sup>17</sup>.

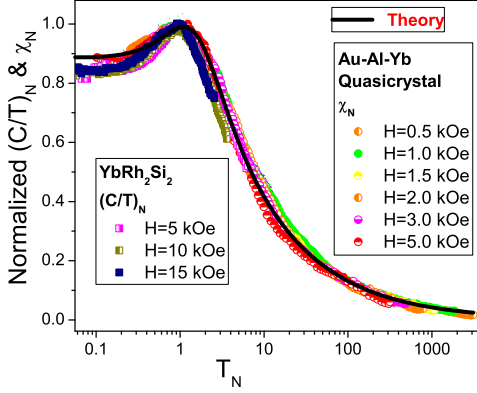


FIG. 2: (color online). The normalized specific heat  $(C/T)_N$  and normalized magnetic susceptibility  $\chi_N$  extracted from measurements in magnetic fields  $H$  on  $\text{YbRh}_2\text{Si}_2$ <sup>21</sup> and on  $\text{Au}_{51}\text{Al}_{34}\text{Yb}_{15}$ <sup>9</sup>, respectively. The magnetic fields are given in the figure. Our calculations are depicted by the solid curve tracing the scaling behavior of  $(C/T)_N = \chi_N = M_N^*$  given by Eq. (10).

To demonstrate this, we apply Eq. (4) to construct  $\varepsilon(p)$  using the functional (11). Taking into account that  $\varepsilon(p \simeq p_F) - \mu \simeq p_F(p - p_F)$  and integrating over the angle variables, we obtain

$$\frac{1}{M^*} = \frac{1}{M} + \frac{\partial}{\partial p} \int [\Phi(p + p_1) - \Phi(|p - p_1|)] \frac{n(p_1, T) p_1 dp_1}{2p_F^2 \pi^2}. \quad (13)$$

Here the derivative on the right hand side of Eq. (13) is taken at  $p = p_F$  and

$$\int_{|p-p_1|}^{p+p_1} V(z, \gamma = 0) z dz = \Phi(p + p_1) - \Phi(|p - p_1|). \quad (14)$$

The derivative  $\partial \Phi(|p - p_1|) / \partial p|_{p \rightarrow p_F} = (p_F - p_1) / (|p_F - p_1|) \partial \Phi(z) / \partial z$  becomes a discontinuous function at  $p_1 \rightarrow p_F$ , provided that  $\partial \Phi(z) / \partial z$  is finite (or integrable if the function tends to infinity) at  $z \rightarrow 0$ . As a result, the right hand side of Eq. (13) becomes proportional  $M^* T$  and (13) reads  $1/M^* \propto M^* T$ , making  $M^* \propto T^{-1/2}$ . Calculations of the corresponding integrals, entering Eq. (13), can be found in textbooks, see e.g.<sup>15</sup>.

The analytic Landau interaction (12) with  $\gamma > 0$  makes  $M/M^* \propto T^{0.5}$  at elevated temperatures, while at

$T \rightarrow 0$  the system demonstrates the LFL behavior<sup>10,16</sup>. This interaction can serve as model one to describe the behavior of the quasicrystal's crystalline approximant  $\text{Au}_{51}\text{Al}_{35}\text{Yb}_{14}$ <sup>9</sup>. The approximant  $\text{Au}_{51}\text{Al}_{35}\text{Yb}_{14}$  shows

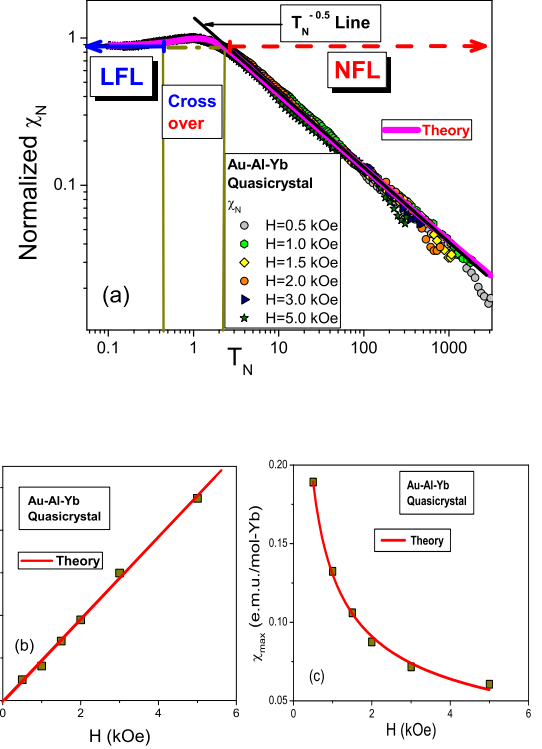


FIG. 3: (color online). (a): Temperature dependence on the double logarithmic scale of the magnetic susceptibility  $\chi_N$  at different magnetic fields<sup>9</sup> shown in the legend. The LFL region and NFL one are shown by the solid and dashed arrows, respectively. The solid line depicts  $\chi_N \propto T_N^{-0.5}$  behavior. (b): The temperatures  $T_{\max}$  at which the maxima of  $\chi$  (see Fig. 1) are located. The solid line represents the function  $T_{\max} = aH$ ,  $a$  is a fitting parameter. (c): The maxima  $\chi_{\max}$  versus magnetic field  $H$ . The solid curve is approximated by  $\chi_{\max} = tH^{-1/2}$ , see Eq. (9),  $t$  is a fitting parameter.

the LFL behavior at low temperatures,  $\chi^{-1} \propto a + bT^{0.51}$  with the conventional LFL behavior of the resistivity<sup>9</sup>. We interpret this behavior of  $\chi^{-1}$  through the absence of the unique electronic state of QCs, which results in the shift of the electronic system of the approximant from FCQPT into the LFL region. Such a behavior is achieved by making the interaction (12) an analytic function with  $\gamma > 0$  as soon as the quasicrystal is transformed into its crystalline approximant. The finite  $\gamma$ , creating the LFL behavior at  $T = 0$ , makes  $T_{\max}$  finite even at  $H = 0$ . Then, it follows from Eq. (10) that  $1/M^* \propto \chi^{-1} \propto a + bT^{1/2}$  and the approximant is to demonstrate the conventional LFL behavior:  $\Delta\rho \propto T^2$ . The same result is acquired by transforming the spectrum



as follows,  $\varepsilon(p) - \mu \propto ([p - p_b]^2 + \gamma^2)(p - p_F)$ <sup>16</sup>.

We now investigate the behavior of  $\chi$  as a function of temperature at fixed magnetic fields. The effective mass  $M^*(T, H)$  can be measured in experiments for  $M^*(T, H) \propto \chi$  where  $\chi$  is the ac or dc magnetic susceptibility. If the corresponding measurements are carried out at fixed magnetic field  $H$  then, as it follows from Eq. (10),  $\chi$  reaches the maximum  $\chi_{\max}$  at some temperature  $T_{\max}$ . Upon normalizing both  $\chi$  and the specific heat  $C/T$  by their peak values at each field  $H$  and the corresponding temperatures by  $T_{\max}$ , we observe from Eq. (10) that all the curves merge into a single one, thus demonstrating a scaling behavior typical for HF metals<sup>10</sup>. As seen from Fig. 2,  $\chi_N$  extracted from measurements on  $\text{Au}_{51}\text{Al}_{34}\text{Yb}_{15}$ <sup>9</sup> shows the scaling behavior given by Eq. (10) and agrees well with our calculations shown by the solid curve over four orders of magnitude in the normalized temperature.

In order to validate the phase diagram Fig. 1, we focus on the LFL, NFL and the transition LFL-NFL regions exhibited by the QC. To this end, we display in Fig. 3 (a) the normalized  $\chi_N$  on the double logarithm scale. As seen from Fig. 3 (a),  $\chi_N$  extracted from the measurements is not a constant, as would be for a LFL. The two regions (the LFL region and NFL one), separated by the transition region, as depicted by the hatched area in the inset of Fig. 1, are clearly seen in Fig. 3 (a) illuminating good agreement between the theory and measurements. The straight lines in Fig. 3 (a) outline both the LFL

and NFL behaviors of  $\chi_N \propto \text{const}$  and  $\chi_N \propto T_N^{-1/2}$ , and are in good agreement with the behavior of  $M_N^*$  displayed in the inset of Fig. 1. In Fig. 3, (b), the solid squares denote temperatures  $T_{\max}(H)$  at which the maxima  $\chi_{\max}$  of  $\chi(T)$  and, (c), the corresponding values of the maxima  $\chi_{\max}(H)$  occur. It is seen that the agreement between the theory and experiment is good in the entire magnetic field domain. It is also seen from Fig. 3 (b) that  $T_{\max} \propto H$ ; thus a tiny magnetic field  $H$  destroys the NFL behavior hereby driving the system to the LFL region. This behavior is consistent with the phase diagram displaced in Fig. 1: at increasing temperatures ( $T_N \simeq 1$ ) the LFL state first converts into the transition one and then disrupts into the NFL state, while at given magnetic field  $H$  the width  $W \propto T$ .

In summary, we have established for the first time that  $\text{Au}_{51}\text{Al}_{34}\text{Yb}_{15}$  quasicrystal exhibits the typical scaling behavior of its thermodynamic properties, and belongs to the famous family of heavy-fermion metals. We have also demonstrated that the quantum critical physics of the quasicrystal is universal, and emerges regardless of the underlying microscopic details of the quasicrystal.

This work was supported by U.S. DOE, Division of Chemical Sciences, Office of Basic Energy Sciences, Office of Energy Research, AFOSR, and by the projects #12-Y-1-1010 of the Ural Division of RAS and #12-P-1-1014 of RAS.

---

\* Electronic address: vrshag@thd.pnpi.spb.ru  
<sup>1</sup> D. Schechtman, I. Blech, D. Gratias, and J. W. Cahn, Phys. Rev. Lett. **53**, 1951 (1984).  
<sup>2</sup> D. Mayou and G. T. de Laissardière, *Quantum transport in quasicrystals and complex metallic alloys*, In Quasicrystals, series Handbook of Metal Physics, (Eds. T. Fujiwara, Y. Ishii, Elsevier Science, 2008), pp. 209-265.  
<sup>3</sup> T. Fujiwara and T. Yokokawa, Phys. Rev. Lett. **66**, 333 (1991).  
<sup>4</sup> T. Fujiwara, in *Physical Properties of Quasicrystals*, (ed. Stadnik, Z. M., Springer, 1999).  
<sup>5</sup> R. Widmera, O. Gröninga, P. Ruffieux, and P. Gröninga, Phil. Mag. **86**, 781 (2006).  
<sup>6</sup> R. Widmer, P. Gröning, M. Feuerbacher, and O. Gröning, Phys. Rev. B **79**, 104202 (2009).  
<sup>7</sup> T. Fujiwara, S. Yamamoto, and G. Trambly de Laissardière, Phys. Rev. Lett. **71**, 4166 (1993).  
<sup>8</sup> G. Trambly de Laissardière, Z. Kristallogr. **224**, 123 (2009).  
<sup>9</sup> K. Deguchi, S. Matsukawa, N. K. Sato, T. Hattori, K. Ishida, H. Takakura, and T. Ishimasa, Nature Materials **11**, 1013 (2012).  
<sup>10</sup> V. R. Shaginyan, M. Ya. Amusia, A. Z. Msezane, and K.

G. Popov, Phys. Rep. **492**, 31 (2010).  
<sup>11</sup> V. R. Shaginyan, Physics of Atomic Nuclei **74**, 1107 (2011).  
<sup>12</sup> V. A. Khodel, J. W. Clark, and M. V. Zverev, Physics of Atomic Nuclei **74**, 1237 (2011).  
<sup>13</sup> L. D. Landau, Sov. Phys. JETP **3**, 920 (1956).  
<sup>14</sup> V. A. Khodel, M. V. Zverev, and J. W. Clark, Phys. Rev. B **71**, 012401 (2005).  
<sup>15</sup> E. M. Lifshitz, L. P. Pitaevskii, *Statistical Physics, Part 1*, (Butterworth-Heinemann, Oxford, 1996) §58.  
<sup>16</sup> J. W. Clark, V. A. Khodel, and M. V. Zverev, JETP Lett. **81**, 315 (2005).  
<sup>17</sup> V. A. Khodel, V. R. Shaginyan, and V. V. Khodel, Phys. Rep. **249**, 1 (1994).  
<sup>18</sup> J. Dukelsky, V. A. Khodel, P. Schuck, and V. R. Shaginyan, Z. Phys. **102**, 245 (1997).  
<sup>19</sup> R. Lifshitz, Z. Phys. **51**, 1156 (2011).  
<sup>20</sup> V. R. Shaginyan, A. Z. Msezane, K. G. Popov, J. W. Clark, M. V. Zverev, and V. A. Khodel, Phys. Rev. B **86**, 085147 (2012).  
<sup>21</sup> N. Oeschler, S. Hartmann, A. P. Pikul, C. Krellner, C. Geibel, and F. Steglich, Physica B **403**, 1254 (2008).